



Wavelet processing and digital interferometric contrast to improve reconstructions from X-ray Gabor holograms

Juan C. Aguilar,^a Masaki Misawa,^{a*} Kiyofumi Matsuda,^a Yoshio Suzuki,^b Akihisa Takeuchi^b and Masato Yasumoto^{b,c}

Received 24 October 2017

Accepted 16 March 2018

Edited by A. Momose, Tohoku University, Japan

Keywords: holography; X-ray microscopy; wavelet transformation.

^aTheranostic Devices Research Group, Health Research Institute, National Institute of Advanced Industrial Science and Technology, AIST, 1-2-1 Namiki, Tsukuba, Ibaraki 305-8564, Japan, ^bJapan Synchrotron Radiation Research Institute / SPring-8, Sayo, Hyogo 679-5198, Japan, and ^cResearch Institute for Measurement and Analytical Instrumentation, NMIJ, National Institute of Advanced Industrial Science and Technology, AIST, Tsukuba, Ibaraki 305-8568, Japan.

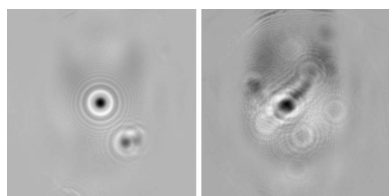
*Correspondence e-mail: m.misawa@aist.go.jp

In this work, the application of an undecimated wavelet transformation together with digital interferometric contrast to improve the resulting reconstructions in a digital hard X-ray Gabor holographic microscope is shown. Specifically, the starlet transform is used together with digital Zernike contrast. With this contrast, the results show that only a small set of scales from the hologram are, in effect, useful, and it is possible to enhance the details of the reconstruction.

1. Introduction

X-ray phase imaging techniques are important tools for observing weak absorbing objects; for example, X-ray holography, Zernike's X-ray microscopy using Fresnel zone plates, the free propagation method, and differential interference contrast (Momose, 2005; Paganin, 2006; Liu *et al.*, 2013; Neuhäusler *et al.*, 2003; Mayo *et al.*, 2002; Kaulich *et al.*, 2002). Digital holography (DH) in visible optics is a valuable tool for observing biological samples. Some biological characterization methods are invasive, but DH does not require a labelling process. In-line versions of DH are possible; for instance, in Sheng *et al.* (2006), the test wave is a plane wave that goes through the sample. Then the approximately undistorted test wave and the scatter wave interfere to produce a hologram. Afterwards, a microscope objective produces the magnification to satisfy the sampling restrictions of the sensor image. Another possibility is described by Garcia-Sucerquia *et al.* (2006); in this case, a spherical wave coming from a pinhole goes through the sample. This setup is similar to that proposed by Gabor (1948), so we will call it the digital Gabor holography microscope (DGBM). The main advantage of the DGBM is that it can be used in different regions of the electromagnetic spectrum such as the terahertz and X-ray regions (Rong *et al.*, 2014; Matsuda *et al.*, 2016).

The main disadvantage of the DGBM is that, even if conventional numerical reconstruction is used to obtain a sharp image, the contrast is still unsatisfactory. This issue appears due to the background and the twin image effect. Reduction of the background is usually carried out with a subtraction of the intensity reference wave or with digital low-pass filtering since it is low-frequency data (Garcia-Sucerquia *et al.*, 2006). Heine *et al.* (2011) applied this method in X-ray holography to observe biological samples. However, as we will



show later, contrast achieved by this method is still not enough to observe details of the object in some other cases. Matsuda *et al.* (2016) showed that digital Zernike contrast can be applied to an X-ray DGBM; however, as in the case of background reduction contrast, minute details still could not be observable because of some additional strong low-frequency information. Wavelet analysis has been applied to DH in diverse ways. Liebling *et al.* (2003) proposed holographic reconstruction in terms of the wavelet basis. This technique is called Fresnelets and has applications for compression and focusing. For image enhancement, wavelet decomposition is useful for regularization of an associate inverse problem (Vonesch & Unser, 2009).

The starlet transform is a wavelet transformation that allows us to express an image in terms of a linear combination of other images, namely the resulting scales and residual. Each image represents a different content in frequency; therefore, we can apply it to a hologram and compute the numerical diffraction of each scale directly. Previously, we performed this analysis and showed some applications to reduce the interferometric noise such as parasitic fringes and the twin image noise (Aguilar *et al.*, 2016). After this processing, we add all the scales except the residual and some scales that represent low frequency. A digital Zernike contrast was used to clarify the performance of twin image denoising in the case of a HeLa cell.

In this work, we extend this application of the starlet transform, which is used to enhance details, by utilizing the digital Zernike phase contrast used by Matsuda *et al.* (2016) and Aguilar *et al.* (2016) in an improved way to observe the most essential information coming from X-ray DGBM holograms, and subsequently enhance the details by performing processes such as unmask sharpening only on the useful scales.

2. Experimental setup in hard X-ray holography and methodology

2.1. Experimental setup

Fig. 1 shows the digital Gabor holographic system in the hard X-ray region. The synchrotron source (beamline 20XU of SPring-8, Japan) used in this study produces quasi-monochromatic X-rays with a monochromator, as shown in Fig. 1. The central part of the expanded X-ray beam is filtered by the aperture CS1 with a size of 50 μm and is focused by a Fresnel zone plate (FZP). The FZP has a three-step quasi-kinofom zone structure made of tantalum. The outermost zone period is 1.2 μm (half pitch of 0.6 μm), and the diameter is 104 μm , which is sufficiently smaller than the spatial coherent length of the illuminating beam. The designed focal length of the FZP is 498 mm at an X-ray wavelength of 0.1259 nm. The measured focus size was 0.6 μm full width at half-maximum, which is equal to the diffraction-limited resolution of the FZP. Another cross-slit aperture CS2 with a size of 2 μm is used to filter the beam and acts as the point source for hologram recording. The beam illuminates the object placed at the distance Z_0 from CS2. The distance between the object and the hologram is Z .

The size of the hologram is determined by the size of the reference beam at the hologram plane (diameter $D = 1.483$ mm at the distance $Z_0 + Z$ from CS2). A 16-bit Hamamatsu charge-coupled device (CCD) sensor (C4742-98-24) with a 3.14 μm pixel size which consists of 1344×1024 pixels was used to record the holograms. Interference fringes with a narrowest spacing of 15.3 μm were produced at the edges of the sensor. The minimum width of the fringe was about 4.9 times the pixel size, thus satisfying the sampling theorem. The X-ray energy was 9.85 keV with a corresponding wavelength of 0.1259 nm. Test samples used in this study were 8 μm polystyrene sphere beads and a HeLa cell.

2.2. Diffraction integral

Because of the quite short wavelength and large distances used in our experiment, it is possible to use Fresnel diffraction or angular spectrum (AS) propagation theory to perform the reconstruction (Goodman, 2005). Another possibility is the so-called Kirchhoff–Helmholtz transform (Jericho & Kreuzer, 2011). However, we prefer AS because, if we assume scalar diffraction, the reconstruction can be performed without any additional approximations. The equation for computing the numerical AS is given by

$$C(x, y) = \mathbf{F}^{-1} \left(\mathbf{F} [H(x, y)] \times \exp \left\{ j \frac{2\pi}{\lambda} z \left[1 - (\lambda f_x)^2 - (\lambda f_y)^2 \right]^{1/2} \right\} \right) \quad (1)$$

where \mathbf{F} and \mathbf{F}^{-1} represent the discrete Fourier transform and its inverse, respectively, x and y represent the discrete variables in the spatial domain, f_x and f_y represent the discrete variables in the frequency domain, $H(x, y)$ is the digital hologram, z is the propagation distance and λ is the wavelength.

2.3. Reconstruction and magnification

For reconstruction in digital holography, we need a reconstruction wave to obtain a sharp image of the object. This reconstruction wave is multiplied by the hologram and, subsequently, the numerical diffraction of this product is computed to simulate the propagation up to some plane where a sharp image of the object is obtained. The reconstruction wave could be the same as the Fresnel approximation of the recording wave produced by the cross-slit CS2; however, it is possible to use other reconstruction waves in order to obtain a specific degree of magnification (Poon & Liu, 2014). Using the original recording wave, the magnification is one and the distance where we obtain a sharp image of the object is the same as the original position of the real object. In our experiment, the sensor image plane is set to $z = 0$ and the other elements are in the negative part of the axis z . If we use a reconstruction wave centered at $-(Z + Z_0)$, the sharp image of the object will be at $Zf = -6.83$ m. If any other wave is used, the reconstruction distance and the magnification values will

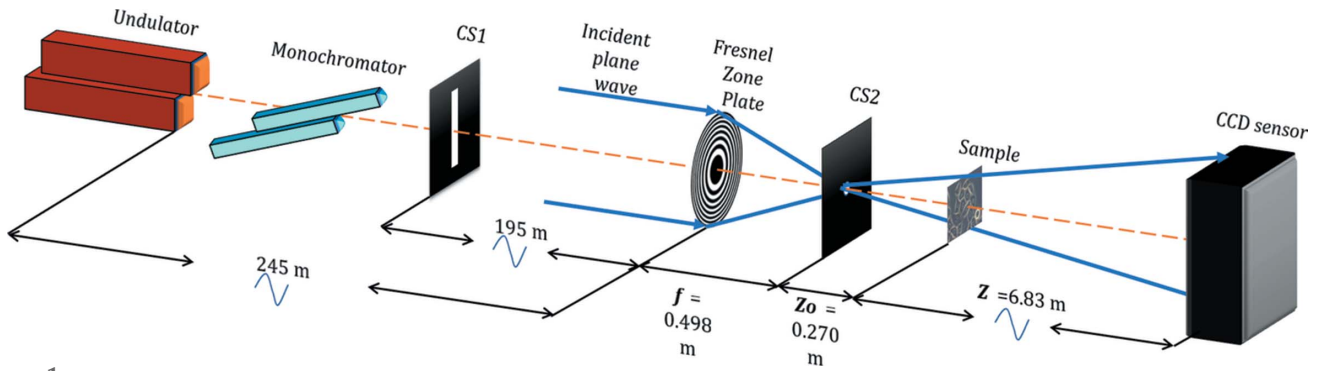


Figure 1
Optical arrangement for the recording of a hard X-ray Gabor hologram. CS1 is a cross-slit aperture for a pseudo-point source of size $50 \mu\text{m} \times 50 \mu\text{m}$, CS2 is a cross-slit aperture for spatial filtering of size $2 \mu\text{m} \times 2 \mu\text{m}$, and FZP is a Fresnel zone plate.

change. In the case of a plane wave, the focus plane Zf and magnification M are given by

$$Zf = -(Z + Z^2/Zo), \quad (2)$$

$$M = (Z + Zo)/Zo. \quad (3)$$

In our experimental setup, we have $Zf \simeq -179.6 \text{ m}$ and $M \simeq 27$.

An important property of using a plane wave in the numerical simulation is that we can begin the simulation of the holographic process using a plane wave as the recording wave, and subsequently derive an equivalent system similar to the experimental system used in this work. For example, if the reconstruction distance is $Zf \simeq -200 \text{ m}$ and the object size is 0.2 mm , then from (2) and (3) this represents a system using a spherical wave centered at $-(Z + Zo) = -7.9 \text{ m}$, with $Z = 7.6 \text{ m}$, $Zo = 0.3 \text{ m}$ and an object size of $1/M = Zo/(Z + Zo) \simeq 0.038$ times the size established in the simulation (that is, a size of around $8 \mu\text{m}$). These values correspond to feasible values for the case of X-ray systems.

2.4. Digital contrast

The reconstruction of $H(x, y)$ at the focus plane is a complex amplitude quantity. Hence, if we add to $H(x, y)$ an additional wave with complex amplitude $A \exp(\alpha)$, where α is a constant in the spatial domain, then the contrast of the resulting intensity image will change. From basic principles of interferometry, the conversion of phase to fringes intensity will be higher if we set $\alpha = \pi/2$, and when we use this value we will refer to it as the digital Zernike contrast. As an example, a simulation for the case of an aspherical object is shown. We assume that it is equivalently represented as a complex distribution located in a single plane which is given by $\Phi = \exp[\varphi(x, y)]$. Following the paraxial approximation, since the rays of an incident plane wave are not refracted significantly, we can use the Radon transform model (Deans, 1993). If the radius of any slice of the spherical object is r , with r_{max} as the highest value, then the phase modification of each slice of the object represented by the corresponding slice of $\varphi(x, y)$ can be modelled as

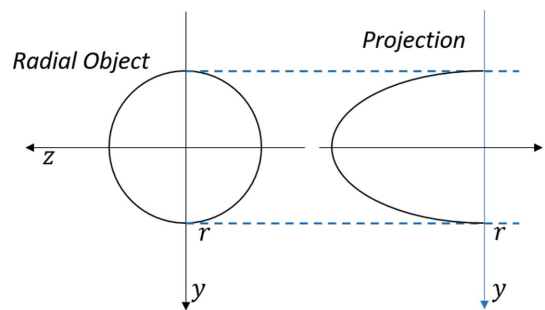


Figure 2
Projection of an object with radial distribution. This model is useful for describing beads where we assume that the contribution of the object is gathered in one plane.

$$\varphi(x, y = \text{constant}) = \begin{cases} 2A(r^2 - x^2)^{1/2}, & |x| \leq r, \\ 0, & \text{otherwise,} \end{cases} \quad (4)$$

where A is a constant. A common graph of any slice of $\varphi(x, y)$ is shown in Fig. 2.

In our simulation, we set $A = \pi/8000$, with a diffraction distance of $Z = 200 \text{ m}$, and the same wavelength as in our experiment. We introduce the digital Zernike contrast element by adding the expression $B \exp(-j\pi/2)$ to the hologram $H(x, y)$, that is, we compute the numerical diffraction in the following form,

$$\mathbf{F}^{-1} \left(\mathbf{F} \left[H(x, y) + B \exp\left(-\frac{j\pi}{2}\right) \right] \right) \times \exp \left\{ j \frac{2\pi}{\lambda} z \left[1 - (\lambda f_x)^2 - (\lambda f_y)^2 \right]^{1/2} \right\}. \quad (5)$$

The result is shown in Fig. 3(c). We can see the different attained kind of contrast compared with the background reduction.

2.5. Wavelet analysis on the hologram

In this section, we will introduce the wavelet transformation used in this work and explain it in terms of the filter banks theory (Proakis & Manolakis, 2006). Wavelet transformation expresses a discrete input signal in terms of other groups of

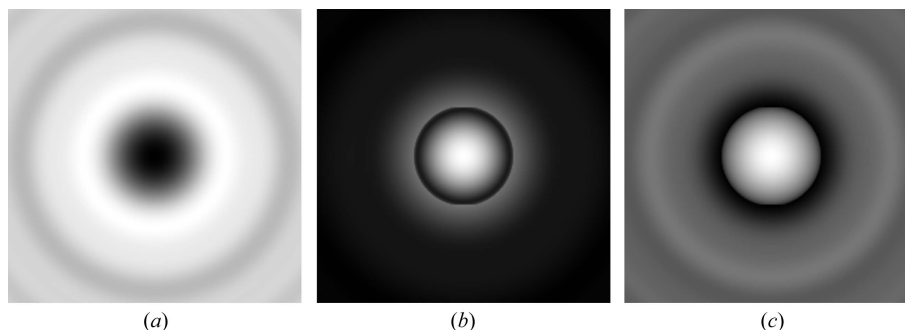


Figure 3 Different reconstructions of a simulated X-ray Gabor hologram of a bead. (a) Normal reconstruction, (b) background reduction, (c) digital Zernike contrast.

signals, called scales, and a signal, called the residual. Each scale and the residual represent a sub-band of the full bandwidth of the input signal. The basic unit used to compute the wavelet transform is shown in Fig. 4(a).

In the figure, the boxes showing h and g represent discrete convolutions, and the boxes showing $N \downarrow$ represent down-sampling operation by N . The filter h is called a low-pass *scaling* filter and g is called a high-pass *wavelet* filter. The spectrum division [using the discrete Fourier transform with $\exp(-j\omega n)$] is shown in Fig. 4(b). Owing to the down-sampling step, the output of each filtering step is a reduced version of the input signal in terms of size. According to the theory of filter banks, it is possible to achieve perfect reconstruction using additional filters, \tilde{h} and \tilde{g} as shown in Fig. 5. All the filters

in this system must satisfy the set of equations given in (6), and the boxes with $N \uparrow$ represent an up-sampling by N ,

$$\hat{h}^*(\omega + \pi) \hat{h}(\omega) + \hat{g}^*(\omega + \pi) \hat{g}(\omega) = 0, \quad (6a)$$

$$\hat{h}^*(\omega) \hat{h}(\omega) + \hat{g}^*(\omega) \hat{g}(\omega) = 1, \quad (6b)$$

where $\hat{\star}$ and \star^* denote the discrete Fourier transform and the complex conjugate, respectively, and equations (6a) and (6b) are called the dealiasing and exact reconstruction equations, respectively. This decomposition can be extended to more scales. The system for two scales and one residual is shown in Fig. 6(a). The transformation makes a bandwidth division as shown in Fig. 6(b), and the same filters \tilde{h} and \tilde{g} help in achieving perfect recovery as shown in Fig. 6(c).

Due to the down-sampling operation, the results obtained in applications of image processing can have some artifacts (Starck *et al.*, 2015). The solution proposed by other researchers was to remove the down-sampling step. This leads to another kind of wavelet transformation called the undecimated or stationary wavelet transformation (Starck *et al.*, 2015). In this case, the size of the scales and the residual are always equal to that of the input signal. Another consequence is that only equation (6b) will be satisfied, because there is no aliasing error. The equivalent undecimated wavelet system for the system in Fig. 6(a) is shown in Fig. 7(a).

The filter $h^{(j)}$ means that we choose a filter h , and $h^{(j)}(n) = h(n)$ if $n/2^j$ is an integer and 0 otherwise. Some examples are shown in Fig. 7(c). The perfect recovery is made using additional filters, \tilde{h} and \tilde{g} , as shown in Fig. 7(b). Because only equation 6(b) must be satisfied, there is more freedom to choose the filters, and a possible selection is

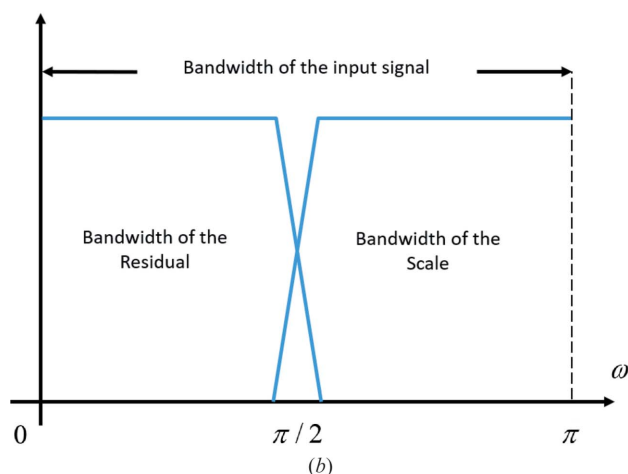
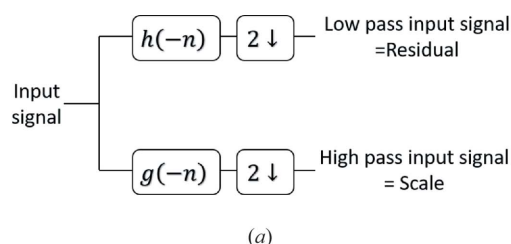


Figure 4 (a) Basic system used to compute a wavelet transform. (b) Bandwidth division of the spectrum of the input signal.

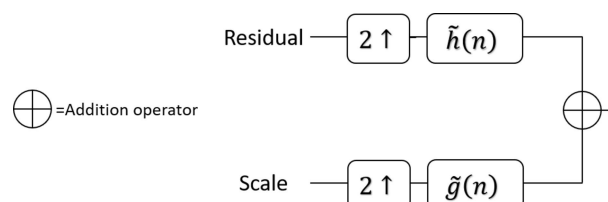


Figure 5 System used to perform perfect recovery of the input signal, using the scale and residual signals.

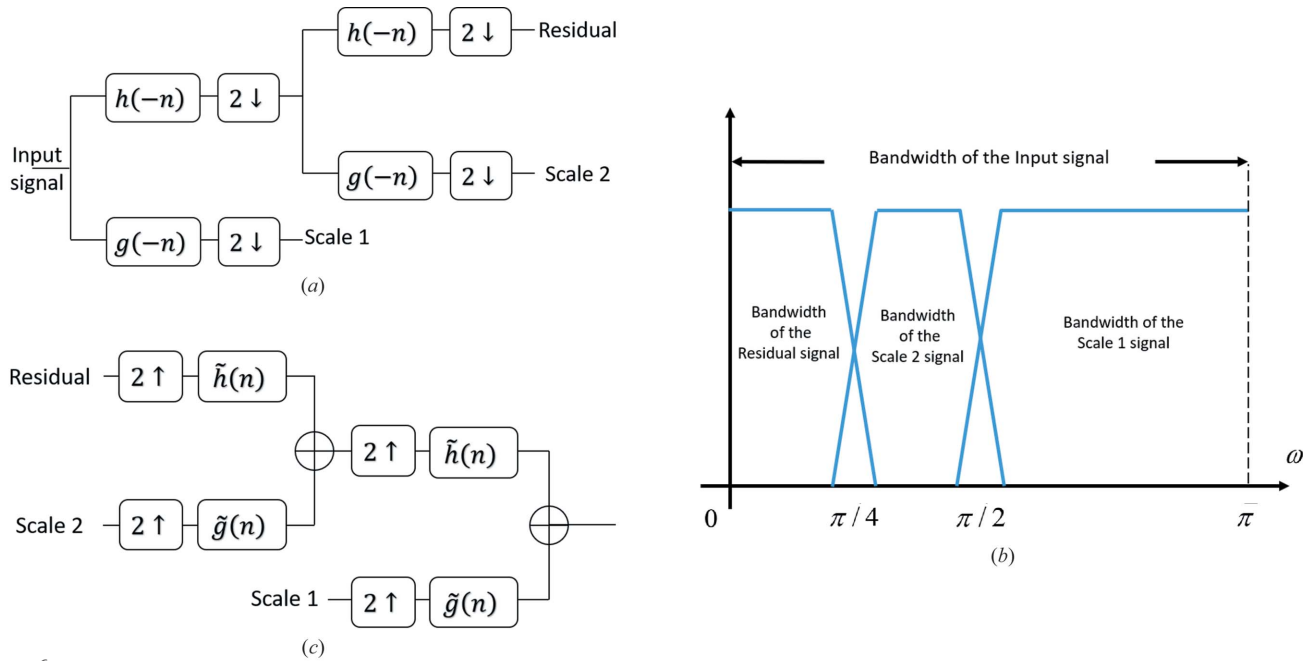


Figure 6 (a) System used to compute a wavelet transformation for two scales and one residual. (b) Bandwidth division of the spectrum of the input signal. (c) System used to perform perfect recovery of the input signal, using two scales and one residual.

$$h(n), g(n) = \delta(n) - h(n), \quad (7)$$

$$\tilde{h}(n) = \tilde{g}(n) = \delta(n), \quad (8)$$

where $\delta(n)$ is the kronecker delta. In order to recover the input signal, the reconstruction system shown in Fig. 7(b) is utilized; we can observe that the reconstruction is performed by addition of the scales and the residual as follows,

$$\begin{aligned} \text{Input signal} &= \text{Residual} + \text{Scale 1} + \text{Scale 2} + \text{Scale 3} \\ &+ \dots + \text{Scale } J. \end{aligned}$$

The above selection of h leads to a transformation called the starlet transform, which has proved to be useful for astronomical processing (Starck *et al.*, 2015), and is used in this study in the context of holography (Aguilar *et al.*, 2016). In the starlet transform, the filter h is given by

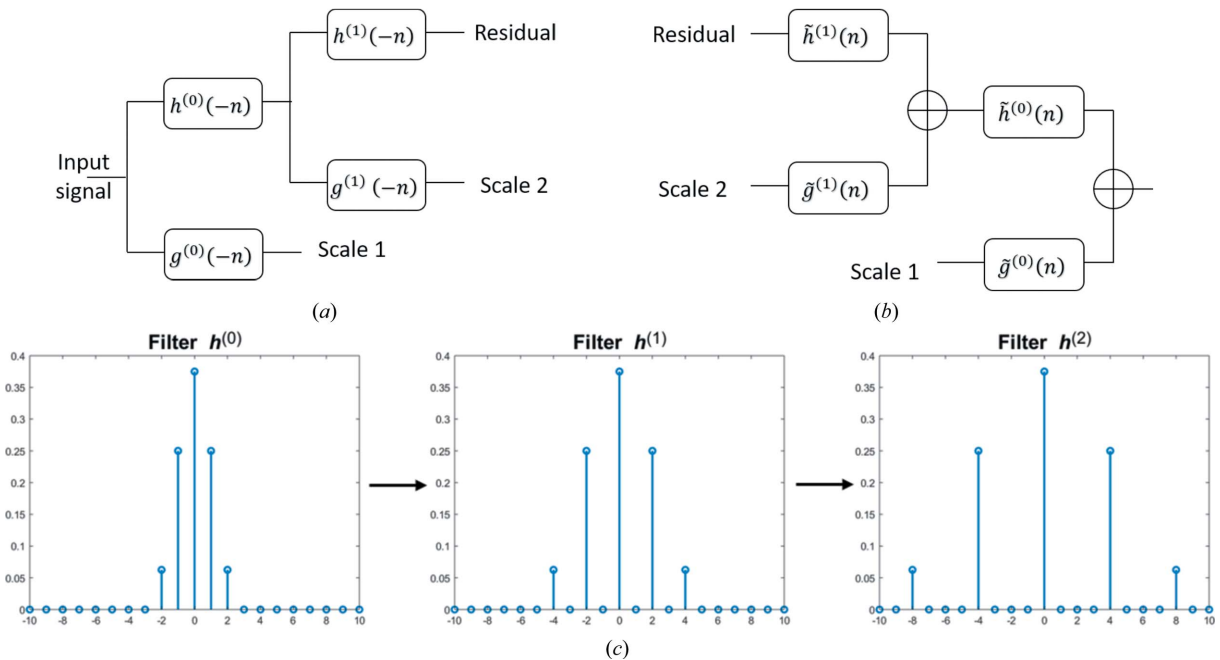


Figure 7 (a) System used to compute the undecimated wavelet transformation for two scales and one residual. (b) System used to perform perfect recovery of the input signal, using the two scales and one residual. (c) Examples of $h^{(j)}$, wherein $h^{(0)}$ is exactly equal to h .

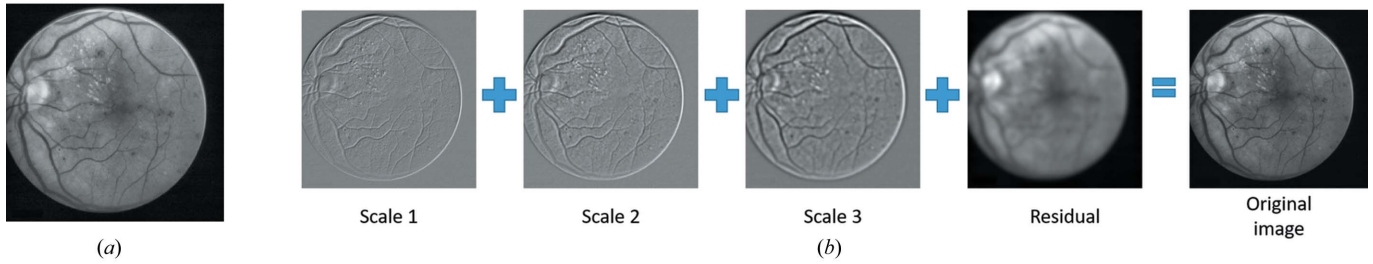


Figure 8 Example of the application of the starlet transform. (a) Ophthalmic medical image. (b) Starlet transform of the image and recovery just by addition of the scales and the residual.

$$h(n) = [1, 4, 6, 4, 1]/16, \quad (9)$$

where $n = -2, \dots, 2$. For images, the starlet transform can be applied similar to the implementation of a two-dimensional discrete Fourier transform (Gonzalez & Woods, 2007; Starck *et al.*, 2015). That is, first, a low-pass filtering is applied in each row of the input image using $h(n)$, and after the same process is performed in the columns we obtain the residual. Next, a high-pass filtering is applied in each row of the input image using $g(n)$, and after the same process is repeated in the columns we obtain scale 1. We repeat the above steps for the residual to obtain scale 2 and a new residual. If we have J scales $W_j[k, l]$, with $j = 1, \dots, J$, and the residual $C_J[k, l]$, then the reconstruction is performed as follows,

$$C_0[k, l] = C_J[k, l] + \sum_{j=1}^J W_j[k, l], \quad (10)$$

where $C_0[k, l]$ is the original image. An example is shown in Fig. 8.

The starlet transform allows us to express a hologram in terms of a linear combination of images, each one representing different content in frequency. Therefore, we can compute the numerical diffraction of each term directly as is shown in (11) and (12) for the case of the scale $W_j(k, l)$ and the residual $C_J(k, l)$, respectively,

$$\mathbf{F}^{-1} \left(\mathbf{F} [W_j(k, l)] \times \exp \left\{ j \frac{2\pi}{\lambda} z \left[1 - (\lambda f_x)^2 - (\lambda f_y)^2 \right]^{1/2} \right\} \right), \quad (11)$$

for $j = 1, \dots, J$, and

$$\mathbf{F}^{-1} \left(\mathbf{F} [C_J(k, l)] \times \exp \left\{ j \frac{2\pi}{\lambda} z \left[1 - (\lambda f_x)^2 - (\lambda f_y)^2 \right]^{1/2} \right\} \right). \quad (12)$$

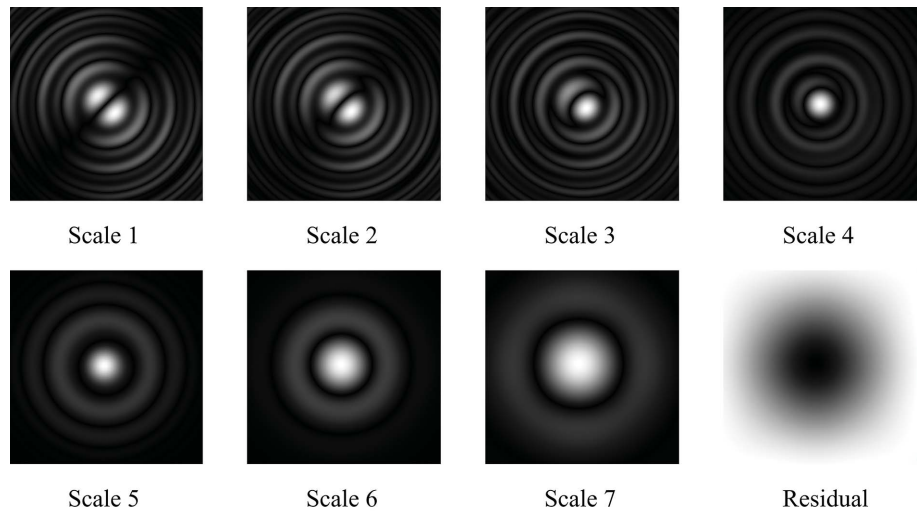


Figure 9 The resulting scales and the residual from the starlet transform of the hologram.

Previously, we performed this analysis and showed some applications to reduce the intrinsic noise such as parasitic fringes and the twin image noise (Aguilar *et al.*, 2016). After this processing, we add all the scales, except the residual and some scales representing low frequency. The digital Zernike contrast was used to clarify the twin image denoising in the case of a HeLa cell sample. In this work, instead of working only on the amplitude information, we will also observe the phase information coming from each scale by applying the Zernike contrast to each of them, as shown in (13). For completeness, we also apply this contrast to the residual,

$$\mathbf{F}^{-1} \left(\mathbf{F} \left[W_j(k, l) + B \exp \left(-\frac{j\pi}{2} \right) \right] \times \exp \left\{ j \frac{2\pi}{\lambda} z \left[1 - (\lambda f_x)^2 - (\lambda f_y)^2 \right]^{1/2} \right\} \right) \quad (13)$$

for $j = 1, \dots, J$.

The results of the starlet transform of $H(x, y)$ and the diffraction of their scales and the residual are shown in Figs. 9 and 10, respectively. The results of applying the Zernike contrast to each diffracted scale and the residual are shown in Fig. 11.

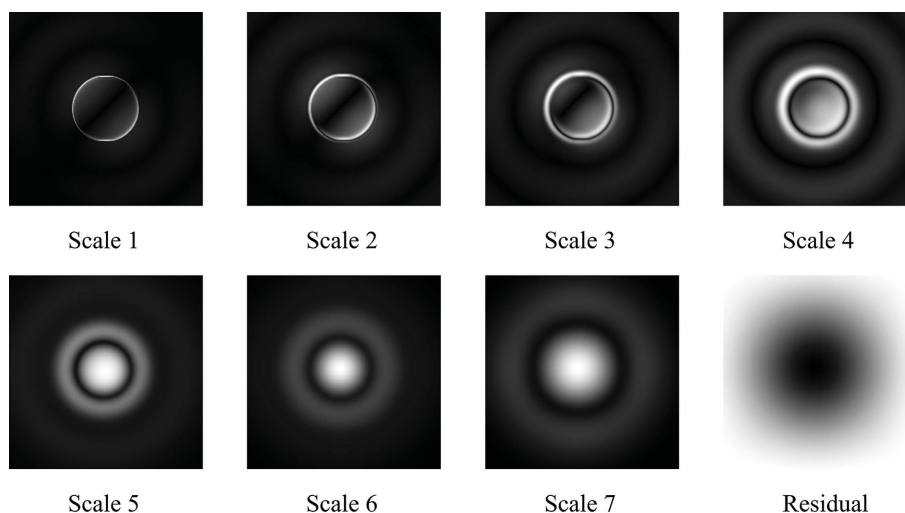


Figure 10
Diffraction of the scales and the residual from the starlet transform of the hologram.

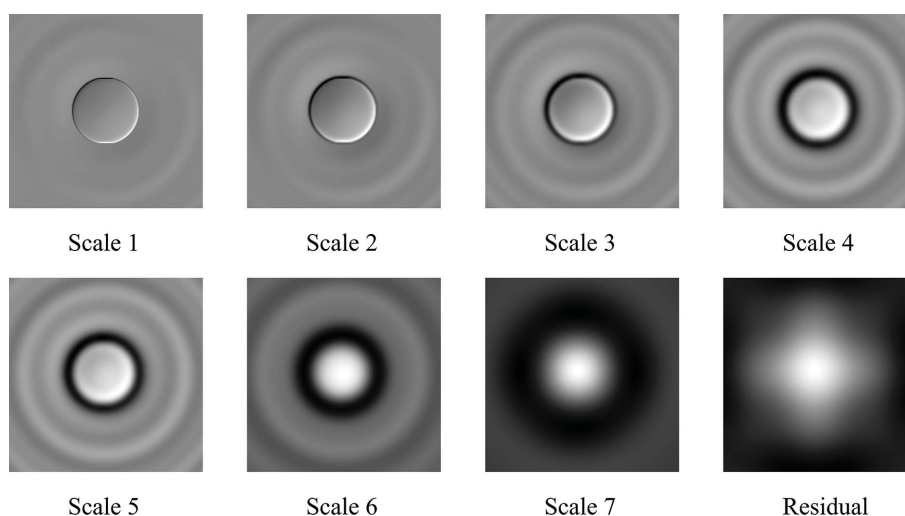


Figure 11
Diffraction of the scales and the residual from the starlet transform of the hologram together with Zernike phase contrast.

From the simulation analysis, we can argue that not all of the information of the scales is useful. For high-frequency information, we can use only one of the three first scales, and

for low-frequency information we can use only one of scales {5, 6, 7}. It is also observed that, since only low-frequency information is contained in the last scales, they do not diffract much, and they are not useful for locating the position of the focal plane. So, we can use only one of the first three scales where it is easy to recognize in which plane the boundary of the object becomes sharp. Such a selection of the scales can be useful not only for symmetric particles but also for more complex objects like cells.

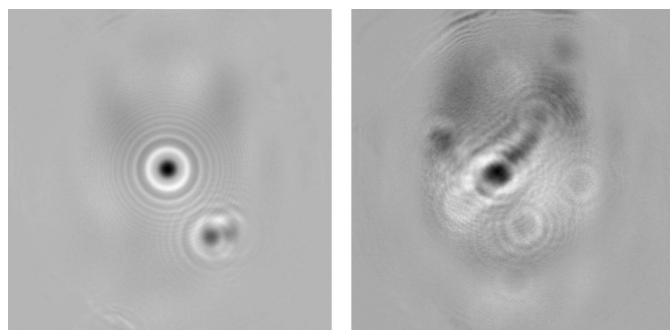


Figure 12
Experimental holograms obtained using the setup shown in Fig. 1. Left: polystyrene beads. Right: HeLa cell.

3. Experimental results and processing

We show the resulting holograms for the case of 8 μm polystyrene beads and human HeLa cells in Fig. 12.

3.1. Polystyrene beads

Normal background erasing contrast and the digital Zernike-type contrast reconstructions, using the full holo-

gram, are shown in Fig. 13. A starlet transform of the hologram is shown in Fig. 14. The diffraction of the scales without and with Zernike contrast are shown in Figs. 15 and 16, respectively. As suggested by the simulation, in the real case, only some scales are useful for analysis. In addition, it is rather easy to find the focal plane using the scale {1} due to the reduction of the parasitic fringes from the twin image.

3.2. HeLa cells

The reconstructions using the full hologram, without any processing, with background reduction, and with the digital Zernike contrast, as shown in (5), are shown in Fig. 17. We can see that Zernike contrast gives a better result, but reduction of the strong low-frequency information is necessary to observe the important details. Next, starlet transform is applied to $H(x, y)$ as before, and the Zernike phase contrast is applied to each diffracted scale. The results are shown in Fig. 18. It is possible to observe that scales {4, 5, 6} do not add important information and can be considered as noise. Scales {3, 7} are good candidates to add details and low-frequency information to the final reconstruction. Then, we add the corresponding hologram scales and apply the digital Zernike contrast as shown in (14),

$$\mathbf{F}^{-1} \left(F \left[W_3(k, l) + W_7(k, l) + B \exp \left(-\frac{j\pi}{2} \right) \right] \times \exp \left\{ j \frac{2\pi}{\lambda} z \left[1 - (\lambda f_x)^2 - (\lambda f_y)^2 \right]^{1/2} \right\} \right). \quad (14)$$

The resulting intensity image is shown in Fig. 19(a). To enhance the reconstruction, we apply a twin image reduction algorithm (Aguilar *et al.*, 2016) to the result of (14). Afterwards, we compute its intensity image and apply an additional unsharpening mask (without histogram equalization) as suggested by Deng (2011). To reduce high-frequency noise, we finally apply a diffusion filtering to preserve the edges. The result is shown in Fig. 19(b). Another possible approach is to enhance the fringes of each scale of the hologram, but this will give a negative effect of strong amplification of the twin image noise in the reconstruction.

4. Discussion of results

HeLa cell reconstruction from the full hologram shows that the background reduction can produce very strong contrast, resulting in possible difficulties in observing additional details of the sample. Therefore, a contrast such as that of the digital

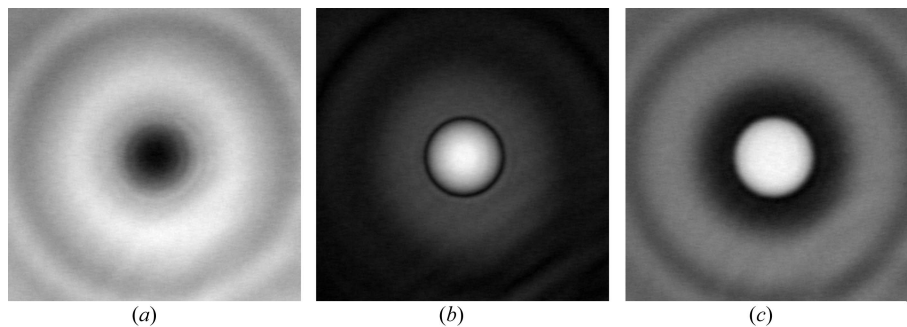


Figure 13 Different reconstructions of an X-ray Gabor hologram polystyrene bead. (a) Normal reconstruction, (b) background reduction, (c) Zernike contrast.

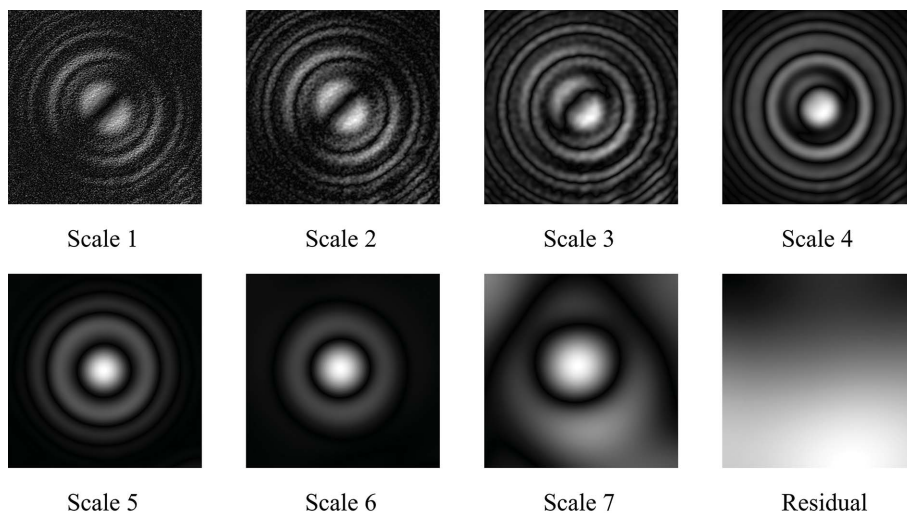


Figure 14 Starlet transform of the 8 μm polystyrene bead hologram.

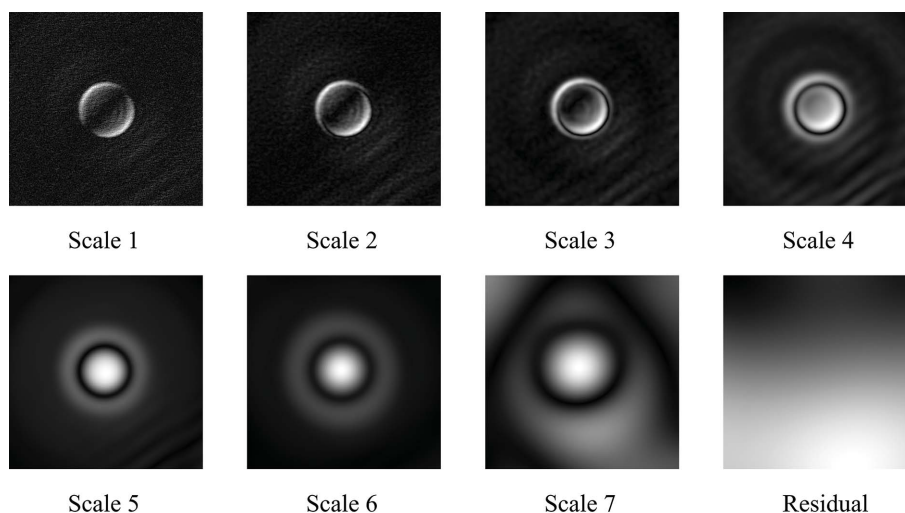


Figure 15
Diffraction of the scales and the residual from the starlet transform of the polystyrene bead hologram.

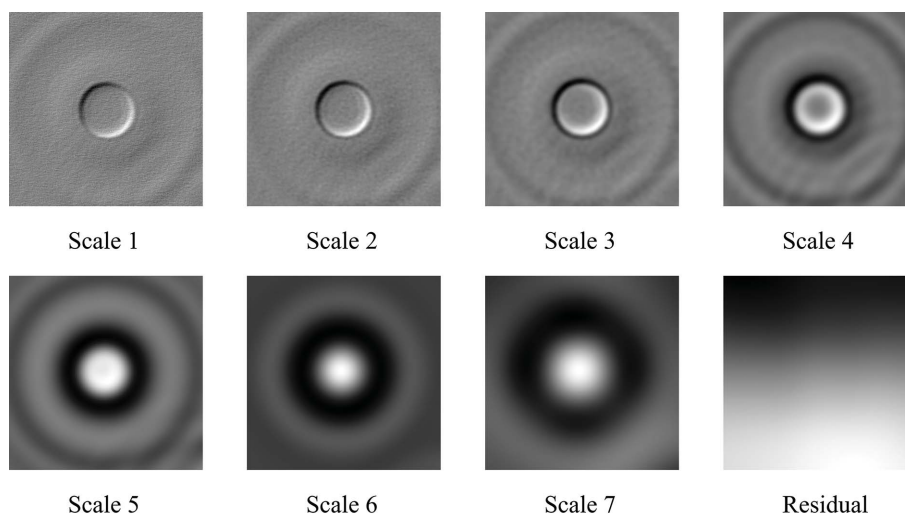


Figure 16
Diffraction of the scales and the residual from the starlet transform of the polystyrene bead hologram together with Zernike phase contrast.

Zernike type is suitable. Nevertheless, the resulting phase image still exhibits a strong low-frequency background, which reduces the visibility of useful detail.

The application of the starlet transform to the hologram makes it possible to enhance the details. Since starlet decomposition enables reconstruction using only the addition of scales and the residual, it is possible to see the contribution of each part of the hologram to the total complex amplitude at the focal plane. However, the absolute value of the diffracted scales appears with very high contrast, which is due to the zero-mean property of the scales W_j . However, when the digital Zernike contrast is applied to each scale, it is easy to estimate the relevance of the information in the case of the HeLa cell.

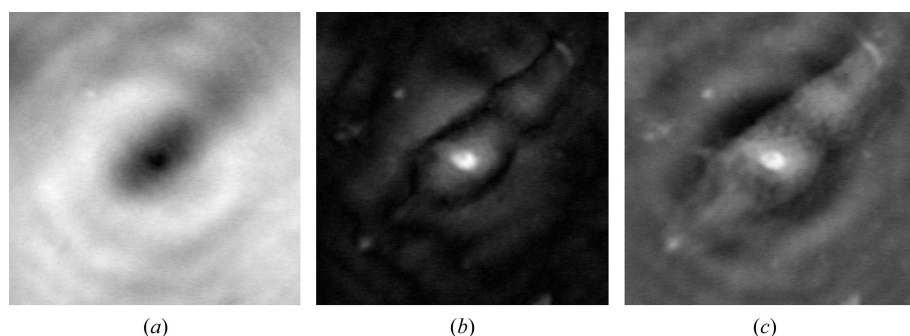


Figure 17
Different reconstructions of the X-ray Gabor hologram of a HeLa cell. (a) Normal reconstruction, (b) background reduction, (c) Zernike contrast.

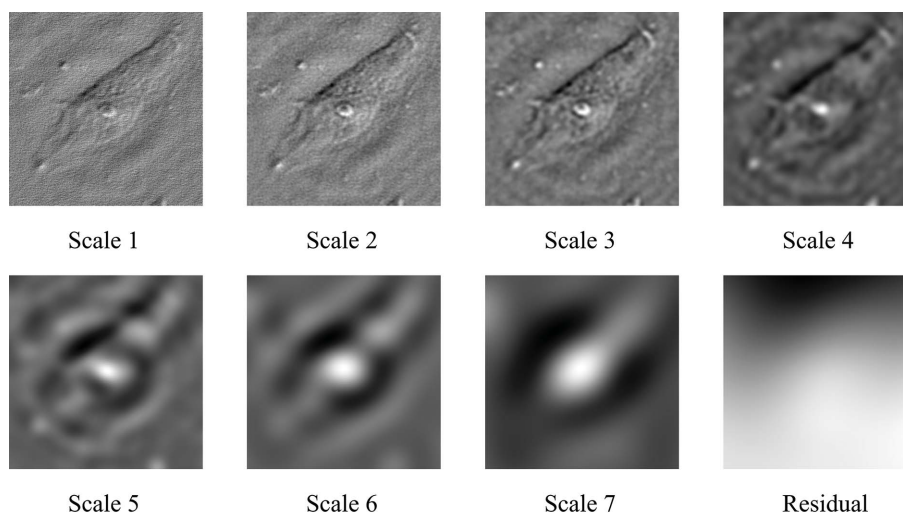


Figure 18
Diffraction of the scales and the residual from the starlet transform of the HeLa cell hologram together with Zernike phase contrast.

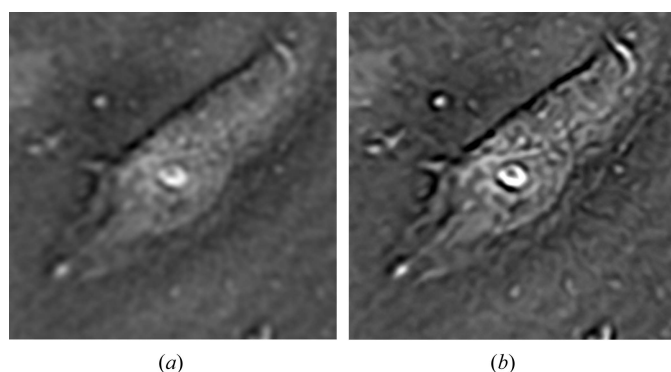


Figure 19
Enhancement of the HeLa cell reconstruction. (a) Scales {3, 7} with Zernike contrast. (b) Enhanced version of (a) using twin image reduction, unsharpening mask and denoising.

5. Conclusions

We have shown a useful tool to improve reconstructions from X-ray holograms. This tool allows us to select which information is valuable for analysis and additional post-processing. Common procedure involves computation of the diffraction of the full hologram. However, by applying the digital Zernike contrast to each scale, we have shown that such a procedure is not the best choice. For instance, not all the scales are necessary to identify the focal plane and observe the details. Our methodology allows us to choose only relevant scales.

Funding information

Funding for this research was provided by: Consejo Nacional de Ciencia y Tecnología (scholarship No. 250204 to JCA); 2016 Saga Prefecture Leading Industry Incubation Program, Japan.

References

Aguilar, J. C., Misawa, M., Matsuda, K., Rehman, S., Yasumoto, M., Suzuki, Y., Takeuchi, A. & Berriel-Valdos, L. R. (2016). *Appl. Opt.* **55**, 6617–6624.

Deans, S. R. (1993). *The Radon Transform and Some of its Applications*. New York: Dover.

Deng, G. (2011). *IEEE Trans. Image Process.* **20**, 1249–1261.

Gabor, D. (1948). *Nature (London)*, **161**, 777–778.

Garcia-Sucerquia, J., Xu, W., Jericho, S. K., Klages, P., Jericho, M. H. & Kreuzer, H. J. (2006). *Appl. Opt.* **45**, 836–850.

Gonzalez, R. C. & Woods, R. E. (2007). *Digital Image Processing*. Upper Saddle River: Pearson.

Goodman, J. W. (2005). *Introduction to Fourier Optics*. Roberts and Company Publishers.

Heine, R., Gorniak, T., Nisius, T., Christophis, C., Pettitt, M. E., Staier, F., Wilhein, T., Rehbein, S., Grunze, M. & Rosenhahn, A. (2011). *Ultramicroscopy*, **111**, 1131–1136.

Jericho, M. H. & Jürgen Kreuzer, H. (2011). *Coherent Light Microscopy*, edited by P. Ferraro, A. Wax, Z. Zalevsky, pp. 3–30. Berlin: Springer.

Kaulich, B., Polack, F., Neuhaeusler, U., Susini, J., di Fabrizio, E. & Wilhein, T. (2002). *Opt. Express*, **10**, 1111–1117.

Liebling, M., Blu, T. & Unser, M. (2003). *IEEE Trans. Image Process.* **12**, 29–43.

Liu, Y., Nelson, J., Holzner, C., Andrews, J. C. & Pianetta, P. (2013). *J. Phys. D*, **46**, 49001.

Matsuda, K., Aguilar, J. C., Misawa, M., Yasumoto, M., Rehman, S., Suzuki, Y., Takeuchi, A. & Niskanen, I. (2016). *J. Eur. Opt. Soc.* **12**, 25.

Mayo, S. C., Miller, P. R., Wilkins, S. W., Davis, T. J., Gao, D., Gureyev, T. E., Paganin, D., Parry, D. J., Pogany, A. & Stevenson, A. W. (2002). *J. Microsc.* **207**, 79–96.

Momose, A. (2005). *Jpn. J. Appl. Phys.* **44**, 6355–6367.

Neuhäusler, U., Schneider, G., Ludwig, W., Meyer, M. A., Zschech, E. & Hambach, D. (2003). *J. Phys. D*, **36**, A79–A82.

Paganin, D. (2006). *Coherent X-ray Optics*. Oxford University Press.

Poon, T. C. & Liu, J. P. (2014). *Introduction to Modern Digital Holography with Matlab*. Cambridge University Press.

Proakis, J. G. & Manolakis, D. K. (2006). *Digital Signal Processing*. Upper Saddle River: Pearson.

Rong, L., Latychevskaia, T., Wang, D., Zhou, X., Huang, H., Li, Z. & Wang, Y. (2014). *Opt. Express*, **22**, 17236–17245.

Sheng, J., Malkiel, E. & Katz, J. (2006). *Appl. Opt.* **45**, 3893–3901.

Starck, J. L., Murtagh, F. & Fadili, J. (2015). *Sparse Image and Signal Processing: Wavelets and Related Geometric Multiscale Analysis*. Cambridge University Press.

Vonesch, C. & Unser, M. (2009). *IEEE Trans. Image Process.* **18**, 509–523.